Supporting Information

# Valence Change Ability and Geometrical Occupation of Substitution Cations Determine the Pseudocapacitance of Spinel Ferrite $XFe_2O_4$ (X = Mn, Co, Ni, Fe)

Chao Wei,[†,⊥,] Zhenxing Feng,[‡,⊥] Murat Baisariyev,[†] Linghui Yu,[†] Li Zeng,[¶] Tianpin Wu,[§] Haiyan Zhao,[‖] Yaqin Huang,[Δ] Michael J. Bedzyk,[¶,#] Thirumany Sritharan,[‡] Zhichuan J. Xu[†,*]

[†]School of Materials Science and Engineering, Nanyang Technological University, 50 Nanyang Avenue, 639798, Singapore;

[‡]School of Chemical, Biological and Environmental Engineering, Oregon State University, Corvallis, Oregon, 97331, United States;

[¶]Graduate Program of Applied Physics, Northwestern University, Evanston, Illinois, 60208, United States;

[#]Materials Science and Engineering, Northwestern University, Evanston, Illinois, 60208, United States;

[§]X-ray Science Divisions, Argonne National Laboratory, Lemont, Illinois, 60439, United States;

[‖]Chemical and Materials Engineering Department, University of Idaho, Idaho Falls, Idaho, 83401, United States;

[Δ]College of Materials Science and Technology, Beijing University of Chemical Technology, Beijing, 100029, P.R. China.

## Experimental details

### Nanoparticle synthesis

The ferrite nanoparticles were synthesized by modified thermal decomposition method.[1] In a typical synthesis of $Fe_3O_4$ nanoparticles, 3 mmol of $Fe(acac)_3$ was dissolved in 15 mL oleylamine. The mixture was firstly maintained at 110 °C for 1 hour, followed by refluxing at 300 °C for 1 hour under Ar atmosphere. Nanoparticle powders were washed with ethanol and hexane by centrifuging at 12000 rpm for 15 minutes. The washing process was repeated for three times to remove the excessive amount of oleylamine. The synthesis of other ferrites ($XFe_2O_4$, X = Mn, Ni, Co) were identical to the method described above but using a molar ratio of 2:1 when feeding $Fe(acac)_3$ and $X(acac)_2$ (X = Mn, Ni, Co) in 15 mL oleylamine. After centrifugation, nanoparticle samples were collected by dispersing in hexane or drying in 80 °C oven for 1 hour.

### Electrode fabrication

Working electrode was prepared by a traditional method.[2,3] Before working electrode fabrication, as-synthesized $XFe_2O_4$ (X = Fe, Co, Ni) powders were calcinated at 300 °C. To tune the inversion degree, as-synthesized $MnFe_2O_4$ was calcinated at 200, 300, and 400 $^oC$ in air for 6 hours. Nanoparticles were then mixed with Vulcan carbon CX72 with a mass ratio of $C:XFe_2O_4$ = 40:60. The as-prepared $C/XFe_2O_4$ ($XFe_2O_4$ = 60 w%) material and polyvinylidene difluoride (PVDF) were mixed in a mass ratio of 90:10 and dispersed in N-methyl pyrrolidone (NMP). The

resulting slurry was pasted onto nickel foam substrate (1 cm × 1 cm) with a spatula. After drying at 80 $^{o}$C for 12 hours, the electrode was pressed at a 10 MPa pressure.

**Electrochemical Characterization**

The electrochemical measurements were performed using the three-electrode method in 1 M $Na_2SO_4$ electrolyte within the potential window of 0 ~ 0.9 V vs Ag/AgCl. Platinum foil and Ag/AgCl electrode (filled with saturated KCl) were used as counter and reference electrodes, respectively. The cyclic voltammetry curves were collected on a Solartron 1287A potentiostat at the scan rate of 5 mV $s^{-1}$. The average specific capacitance was calculated by the following formula:

$$C_{avg} = \Delta Q/w\Delta V = \left(\int IdV\right)/s/\Delta V/w$$

where $\Delta Q$ is the total amount of charge accumulated over a potential window $\Delta V$, $w$ is the mass of the active material, $s$ is the voltage scanning rate and $I$ is the current.

Each data point and its error bar were obtained by three independent measurements. The specific capacitance (F/g) of spinel oxides was calculated after subtracting the maximum contribution from carbon according to the weight ratio of oxide to carbon.[3,4] The capacitance of pure Vulcan carbon was experimentally determined to be 12.3 F/g. The specific capacitance (μF/$cm^{-2}$) of spinel oxides was estimated by normalizing the charge to oxide surface area.

**Materials Characterization**

TEM characterization and size analysis on ferrite nanoparticles were performed on a JEOL 2010 transmission electron microscope (TEM) at 200 kV. The number-average width $W_n$, was calculated as follows:

$$dW_n = \frac{\sum_{i=1}^{n} dW_i}{n}$$

where $W_i$ is the diameter of individual nanoparticle, $n$ is the number of counted nanoparticle. $W_i$ was determined by averaging the length measured at two different directions that are perpendicular to each other. XRD patterns of $MnFe_2O_4$ calcinated at different temperatures were collected by Shimadzu (thin film) with a Cu Kα radiation (λ = 1.5418 Å). BET surface area was measured by a ASAP Tri-star II 3020 machine. To ensure the accurate estimation of surface area, at least 250 mg samples were loaded for analysis.

**X-ray absorption spectroscopy**

Synchrotron X-ray diffraction (XRD) was carried out at beamline 33BM-C of the XOR Division, at Advanced Photon Source (APS) at Argonne National Lab (ANL) using 20 keV X-rays with incident flux of ~$10^{10}$ photons/s. Scattered X-rays were detected using a pixel array area detector (Dectris PILATUS 100 K model).

In-situ XANES and EXAFS experiments were carried out at beamline 9BM-C of the XOR Division, APS, ANL. The working electrodes were made on 100-μm thick graphite papers. The

working electrode was mounted onto a custom-designed in-situ XAS backscattering fluorescence cell (Figure S6). The cell is setup for the three-electrode measurements and can contain up to 30 mL electrolyte. Gold wire and Ag/AgCl electrode (filled with saturated KCl solution) were used as counter and reference electrodes, respectively. All data were collected in fluorescence mode under applied potential controlled by a CHI 660E electrochemical workstation. A Lytle detector was used to collect the X (X=Ni, Co, and Mn) and Fe K fluorescence signal while the Si(111) monochromator scanned the incident X-ray photon energy through the M and Fe K absorption edge. The monochromator was detuned to 80% of the maximum intensity at those X and Fe K edges to minimize the presence of higher harmonics. XAS measurements were done at different applied potentials. The X-ray beam was calibrated using the Pt metal foil K edge at 9442 eV.

Data reduction and data analysis were performed with the Athena, Artemis and IFEFFIT software packages. Standard procedures were used to extract the EXAFS data from the measured absorption spectra. The pre-edge was linearly fitted and subtracted. The post-edge background was determined by using a cubic-spline-fit procedure and then subtracted. Normalization was performed by diving the data by the height of the absorption edge at 50 eV. Experimental phase shifts and back-scattering amplitudes were obtained from reference samples, which were also used to determine the best fit of Debye-Waller factors (DWF) and amplitude reduction factors ($S_0$) for phase shifts and back-scattering amplitudes in the FEFF fitting. Typical values for the limits of accuracy of the EXAFS coordination parameters are: $N$ (± 10%), $R$ (± 5%),$\sigma^2$ (± 10%) and $E_0$ (± 10%).

**EXAFS fitting**

For each $XFe_2O_4$ spinel ferrites, EXAFS spectra are recorded on both X (X = Mn, Co, Ni) and Fe K edges and each edge has a theoretical standard. It is worth noting that the EXAFS fitting of two elements are conducted simultaneously in order to accurately extract the quantative information of site occupancy. This method has been employed in previous studies. Theoretical models in this study were built by *ab initio* calculations on FEFF8.[5] A cubic spinel crystal frame (space group 227) was used. Considering the tremendous number of scattering paths within the fitting range (from 1 Å to ~4 Å), we made several constraints and approximation by referencing a landmark work.[5]

A theoretical standard was calculated for the tetrahedral and octahedral environments for each of the two elements, giving four standards in total. The site occupancy can be described by one varaiable, $x_A$(X), i.e., the number of X (X = Mn, Co, Ni) at tetrahedral sites. According to the stoichiometry, $x_B$(X) = 1 - $x_A$(X), $x_A$(Fe) = 1 - $x_A$(X), $x_B$(Fe) = 1 + $x_A$(X). The coordination number was obtained by setting $S_0^2$ to the value detemined from the standard reference sample. For exampe, bulk $Fe_3O_4$ serves as the reference sample for all Fe edges; $Mn_3O_4$ for Mn; $Co_3O_4$ for Co and NiO for Ni. The model validity was confirmed by two commonly used parameters: $R$ factor and $\chi_\upsilon^2$ (Table S2).[5,6,7] It should be noted that the values of $R$ and $\chi_\upsilon^2$ in this work are much smaller than some previous reports,[5,7,8] validating the rationality of our model.

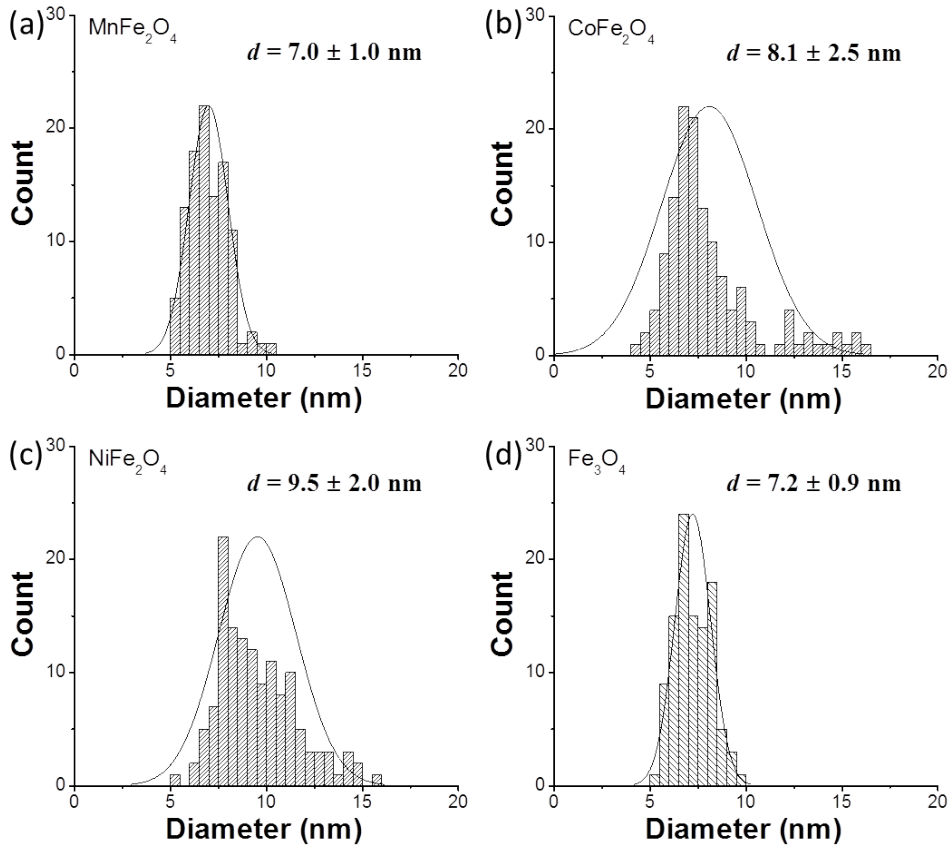


**Figure S1**. Size distribution of carbon supported ferrite nanoparticles: (a) $MnFe_2O_4$, (b) $CoFe_2O_4$, (c) $NiFe_2O_4$, and (d) $Fe_3O_4$.

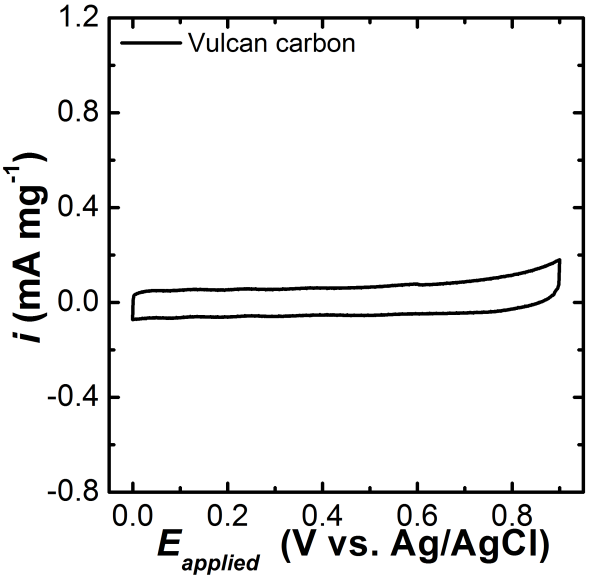


**Figure S2**. CV scans of vulcan carbon at the scan rate of 5 mV/s.

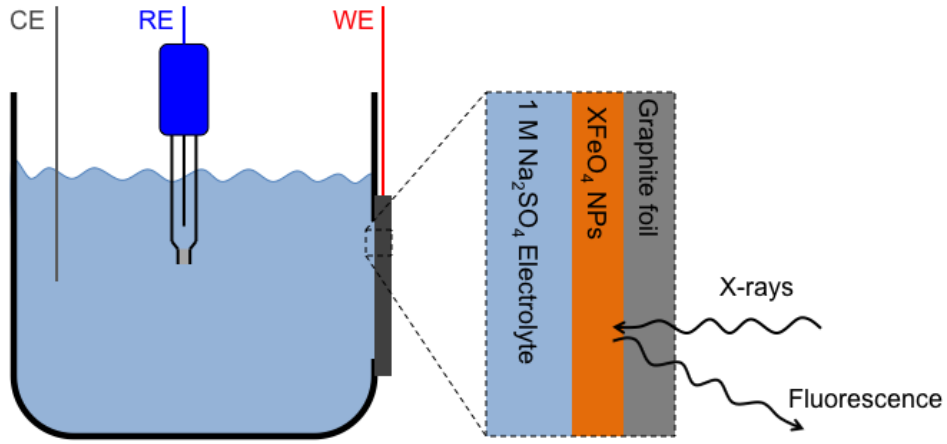


**Figure S3**. In-situ XAS setup used in experiments, with the one side of the graphite foil facing the incoming X-ray and the other side with deposited $XFe_2O_4$ nanoparticles (NPs) in contact with 1 M $Na_2SO_4$ electrolyte. CE, RE, and WE stand for counter, reference and working electrodes, respectively.

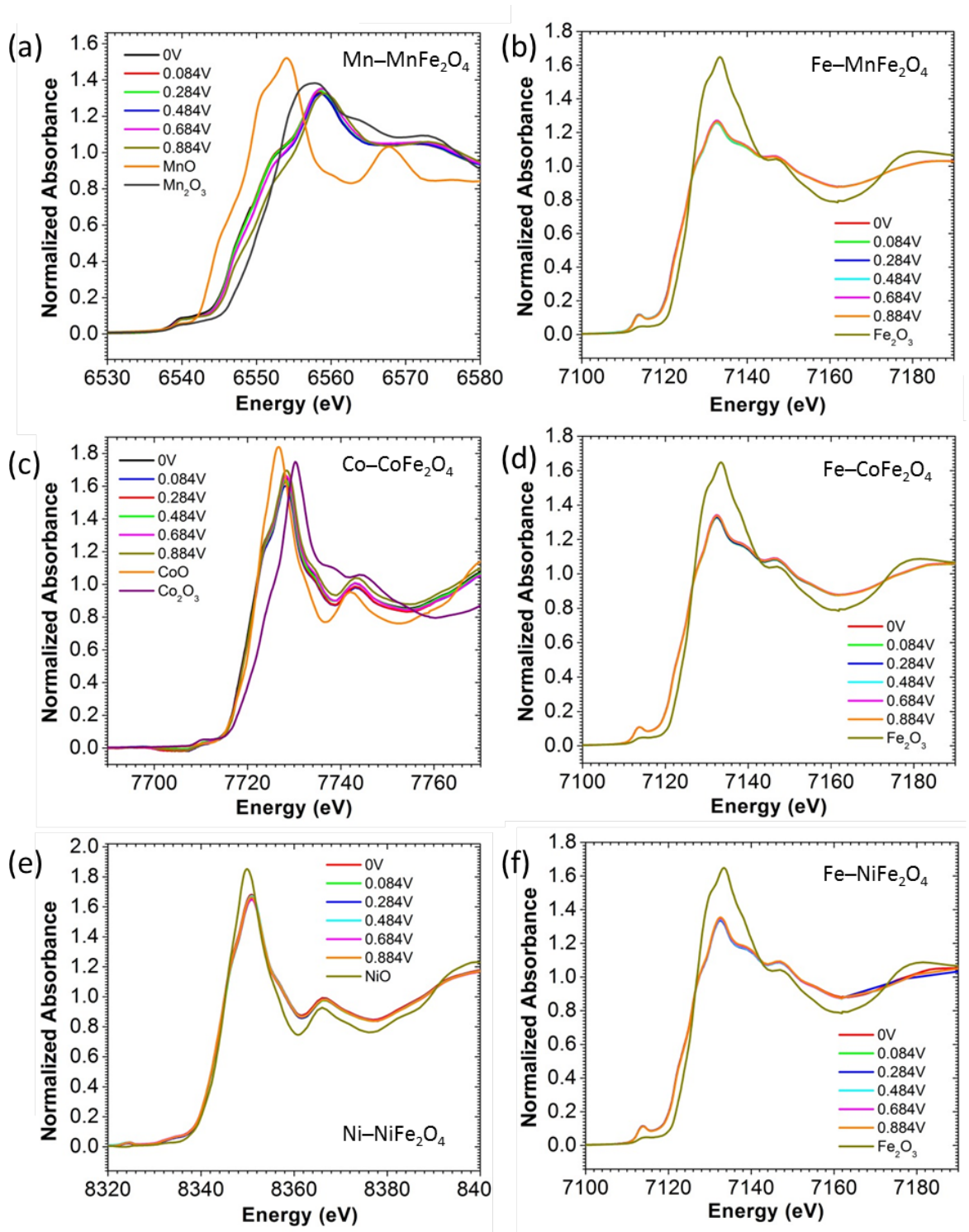


**Figure S4**. In-situ XANES spectra of $XFe_2O_4$: (a) $MnFe_2O_4$ (b) $CoFe_2O_4$; (c) $NiFe_2O_4$.

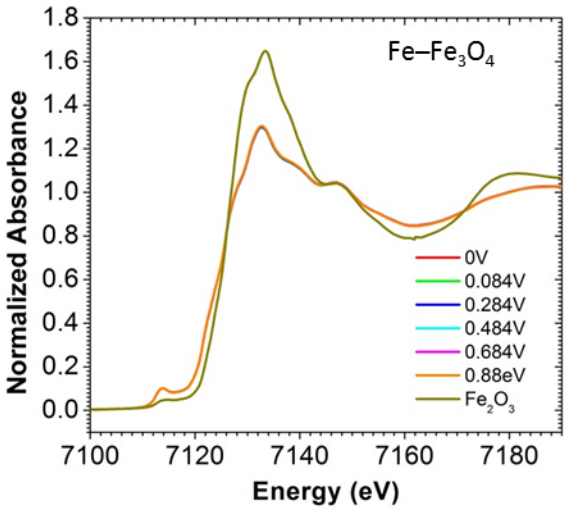


**Figure S5**. In-situ XANES spectra of $Fe_3O_4$. The applied potential does change the Fe edge position, which still almost overlaps with $Fe^{3+}$.

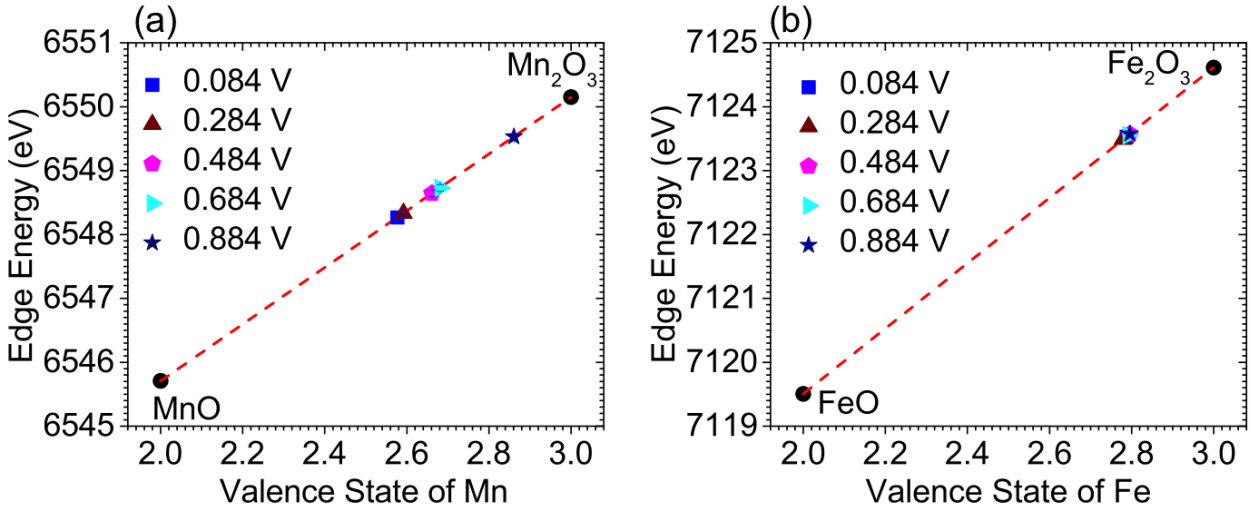


**Figure S6**. (a) The Mn and (b) Fe valence states of $MnFe_2O_4$ under different applied potentials are linearly interpolated from their corresponding reference, MnO and $Mn_2O_3$ for Mn, and FeO and $Fe_2O_3$ for Fe.

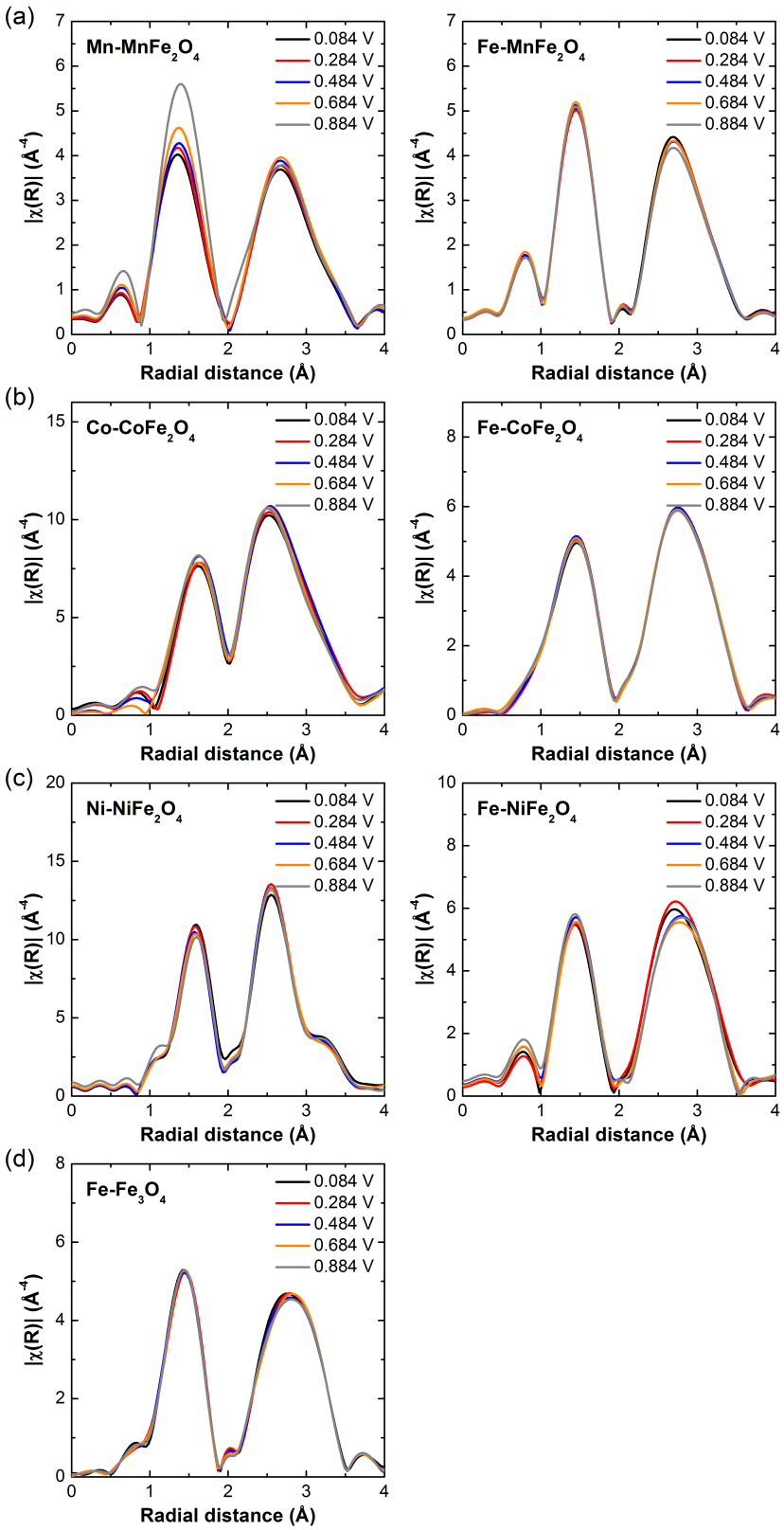


**Figure S7**. In-situ EXAFSspectra of $XFe_2O_4$: (a) $MnFe_2O_4$ (b) $CoFe_2O_4$; (c) $NiFe_2O_4$; (d) $Fe_3O_4$ with increasing applied potential.

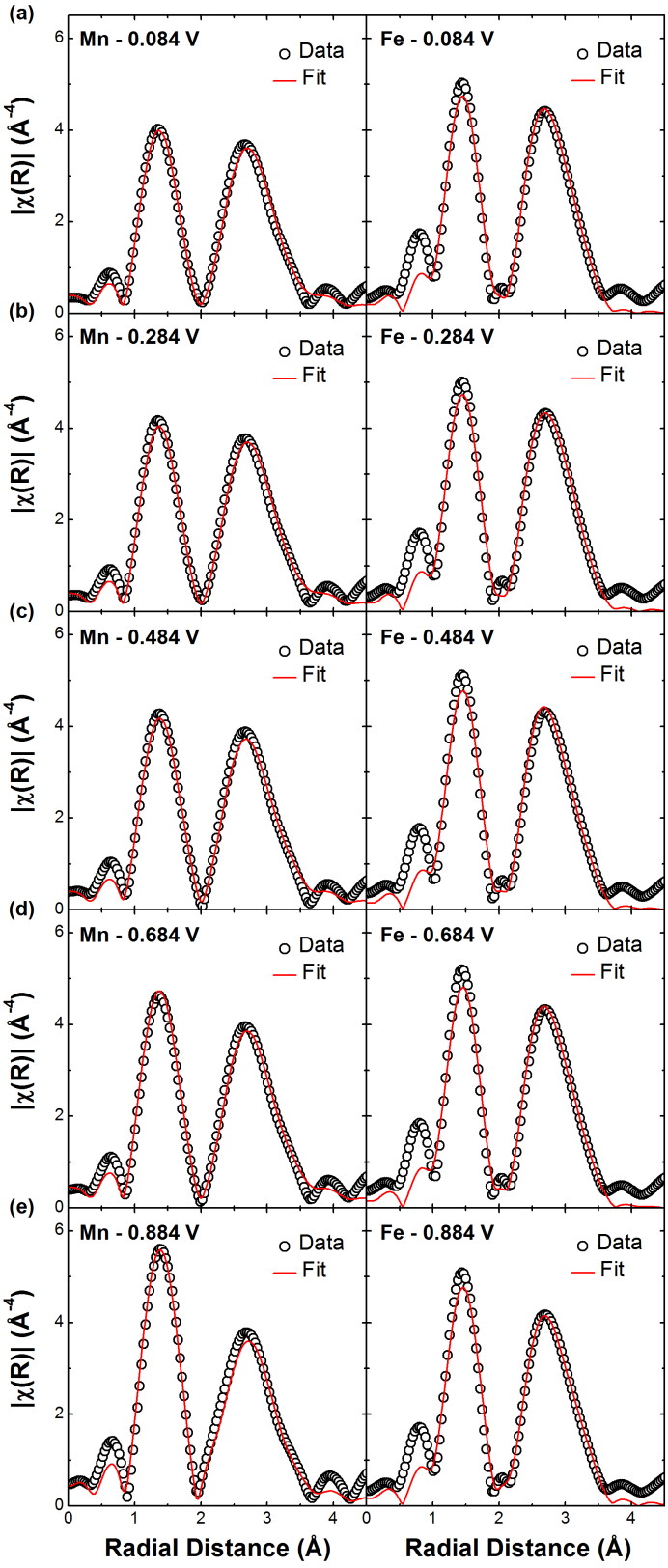


**Figure S8**. In-situ EXAFS $k^3\chi(R)$ spectra and fitting results at Mn and Fe K edge. (a) 0.084 V; (b) 0.284 V; (c) 0.484 V; (d)0.684 V; (d) 0.884 V.

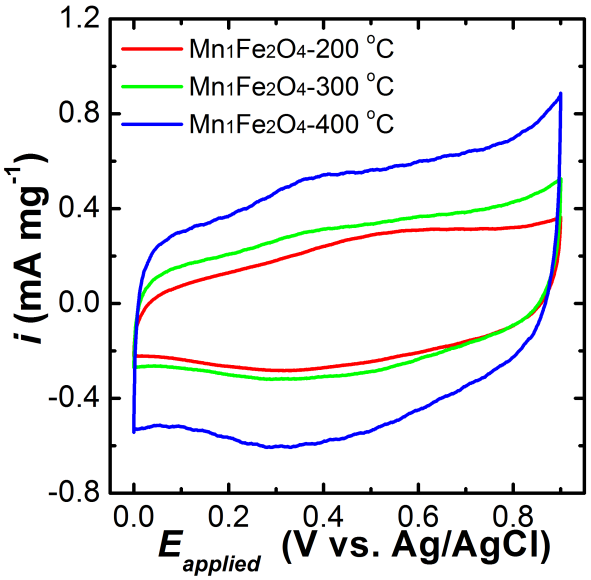


**Figure S9**. CV scans of $Mn_1Fe_2O_4$ - 200 °C, $Mn_1Fe_2O_4$ - 300 °C and $Mn_1Fe_2O_4$ - 400 °C at the scan rate of 5 mV/s.

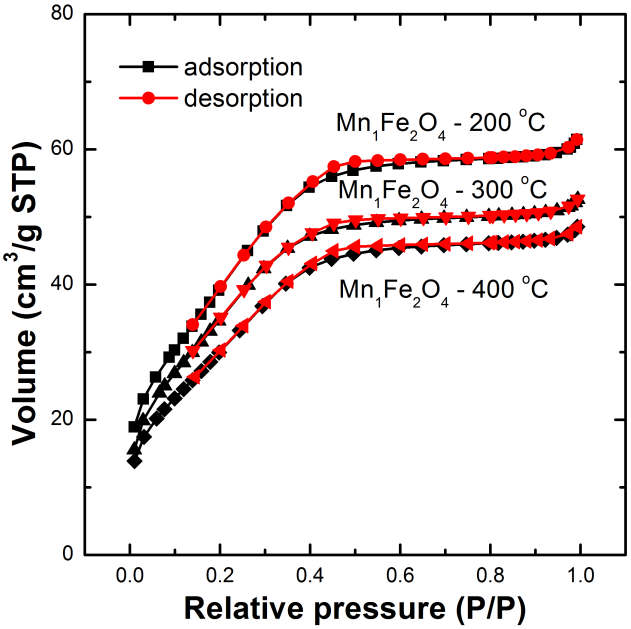


**Figure S10**. BET measurements of $Mn_1Fe_2O_4$ - 200 °C, $Mn_1Fe_2O_4$ - 300 °C and $Mn_1Fe_2O_4$ - 400 °C. Detailed results are given in Table S3.

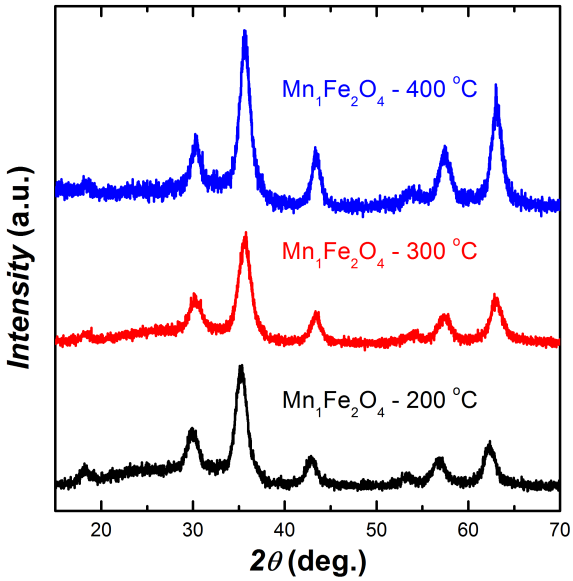


**Figure S11**. XRD patterns of $Mn_1Fe_2O_4$ calcinated at different temperatures.

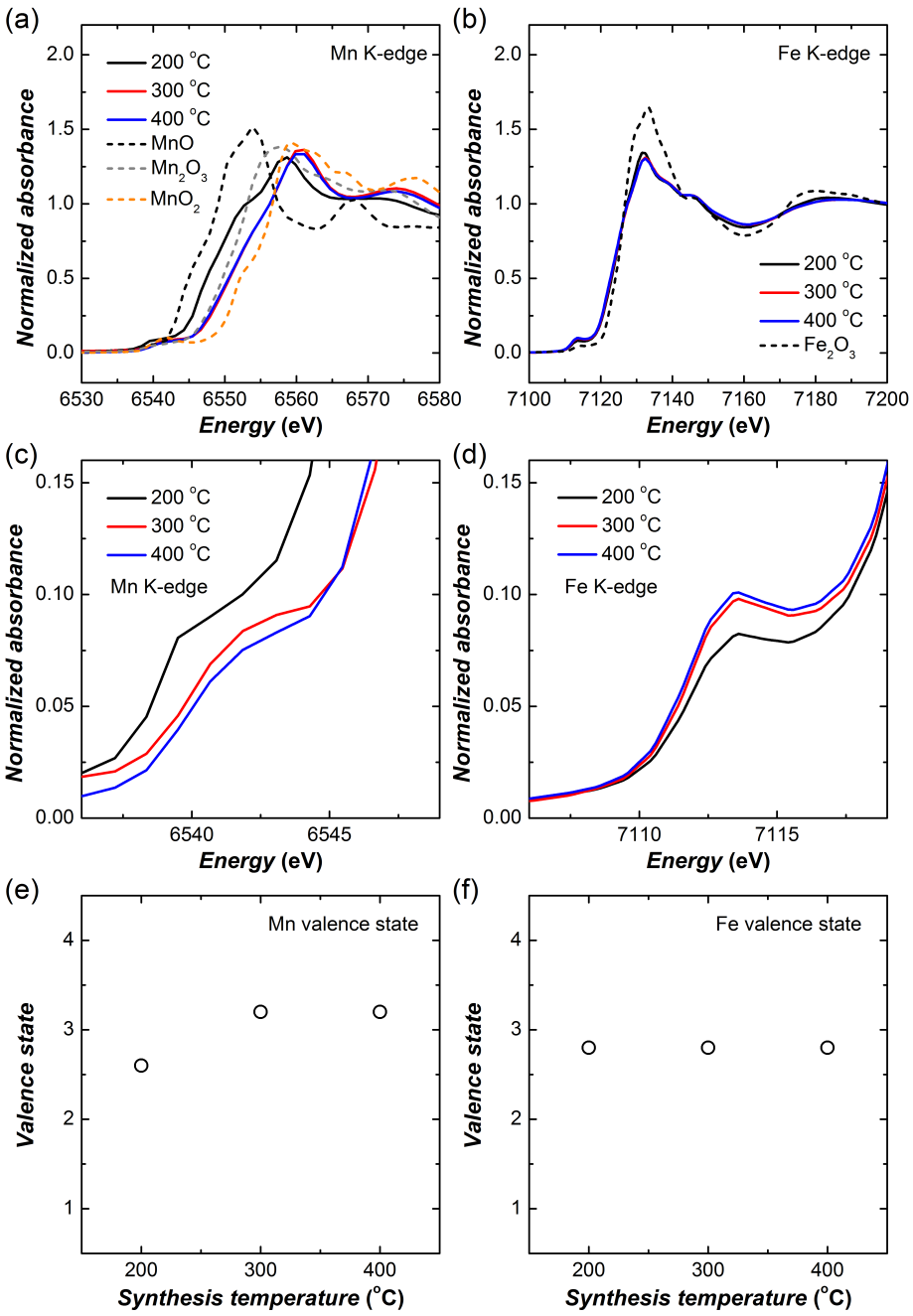


**Figure S12**. XANES spectra of (a) Mn and (b) Fe K-edge at $MnFe_2O_4$ calcinated at different temperatures. XANES pre-peaks of (c) Mn and (d) Fe K-edge at $MnFe_2O_4$ calcinated at different temperatures.Valence state of (e) Mn and (f) Fe K-edge at $MnFe_2O_4$ calcinated at different temperatures.

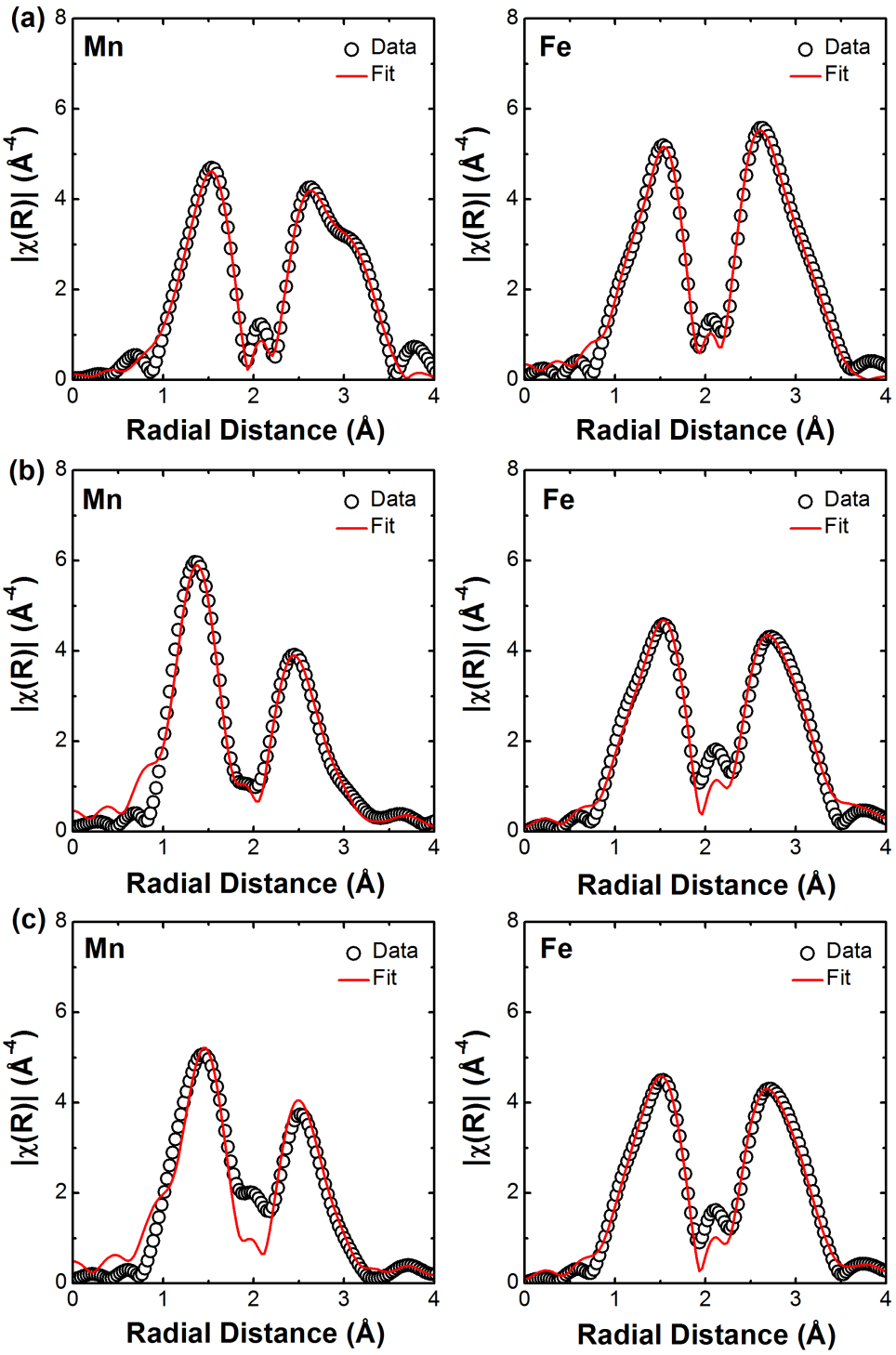


**Figure S13**. EXAFS $k^3\chi(R)$ spectra and fitting results at Mn and Fe K edge. (a) $Mn_1Fe_2O_4$ - 200 $^oC$; (b) $Mn_1Fe_2O_4$ - 300 $^oC$; (c) $Mn_1Fe_2O_4$ - 400 $^oC$.

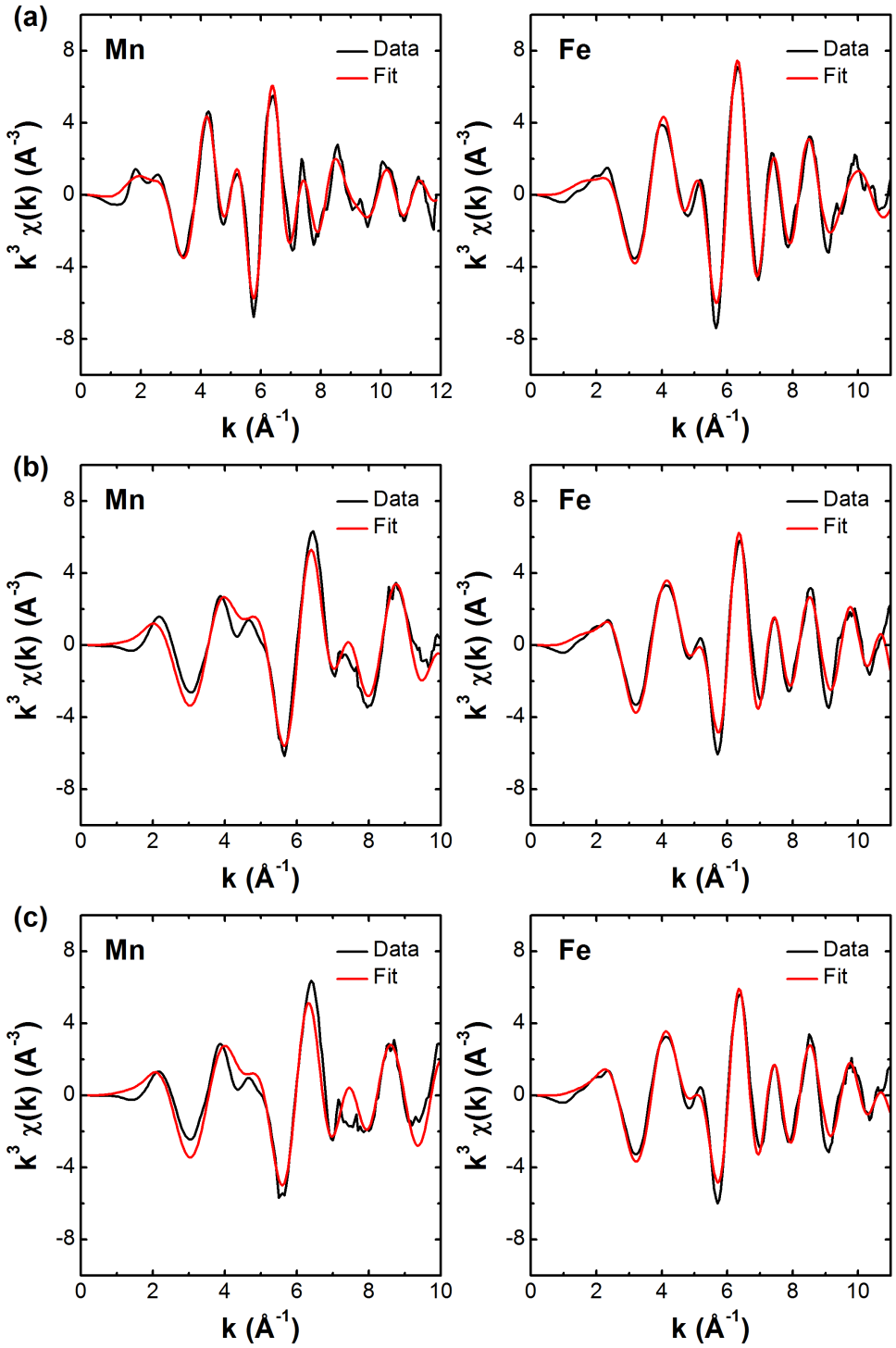


**Figure S14**. EXAFS $k^3\chi(k)$ spectra at Mn and Fe K edge. (a) $Mn_1Fe_2O_4$ - 200 °C with a fitting range of 2~11 Å$^{-1}$ for Mn and 2~11 Å$^{-1}$ for Fe. (b) $Mn_1Fe_2O_4$ - 300 °C with a fitting range of 2~10 Å$^{-1}$ for Mn and 2~10 Å$^{-1}$ for Fe. (c) $Mn_1Fe_2O_4$ - 400 °C with a fitting range of 2~10 Å$^{-1}$ for Mn and 2~10 Å$^{-1}$ for Fe.

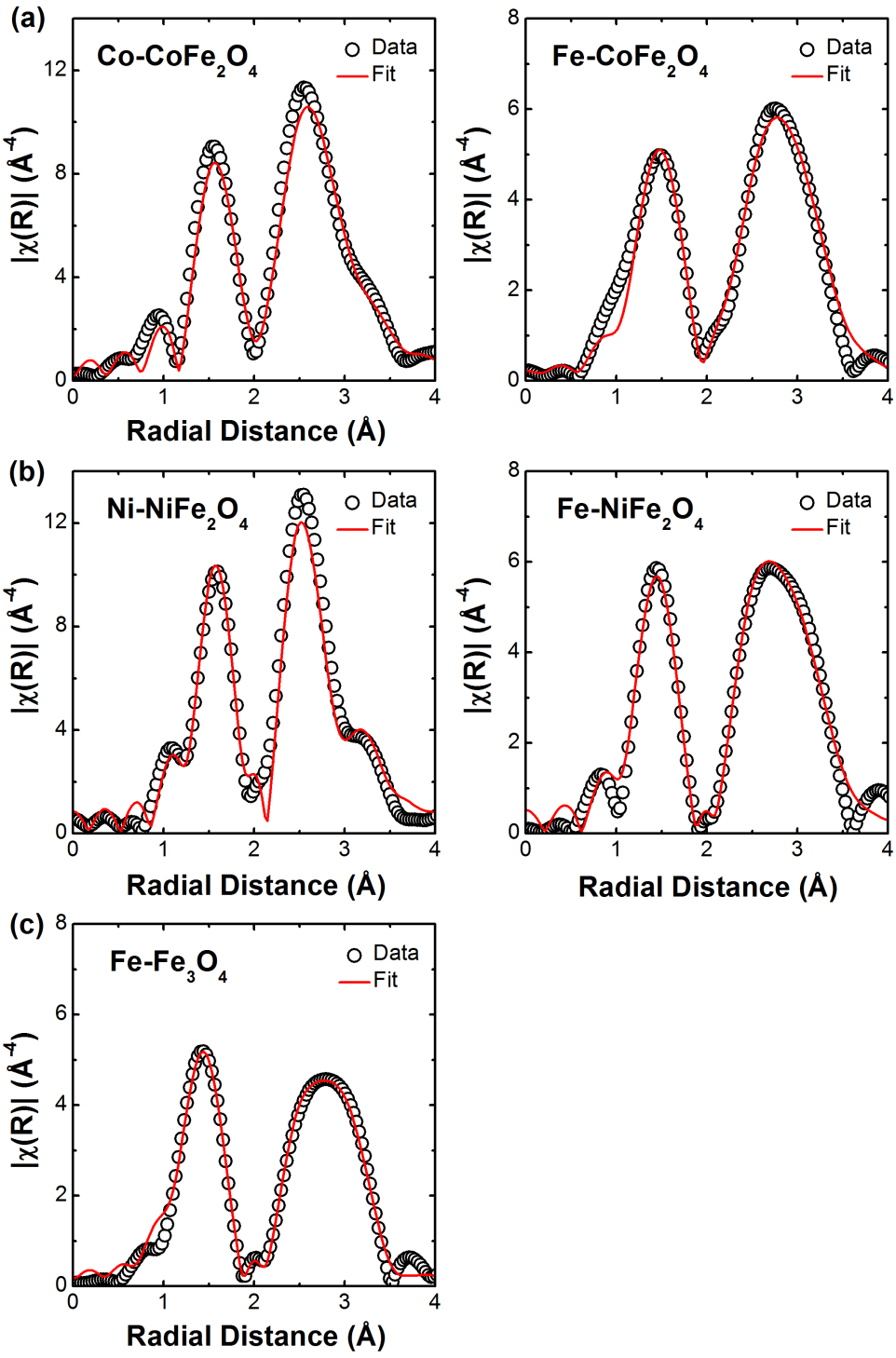


**Figure S15**. EXAFS $k^3\chi(R)$ spectra and fitting results of (a) $CoFe_2O_4$; (b) $NiFe_2O_4$; (c) $Fe_3O_4$. Co and Ni have strong preference for octahedral site, which is consistent with previous findings.[7,9]

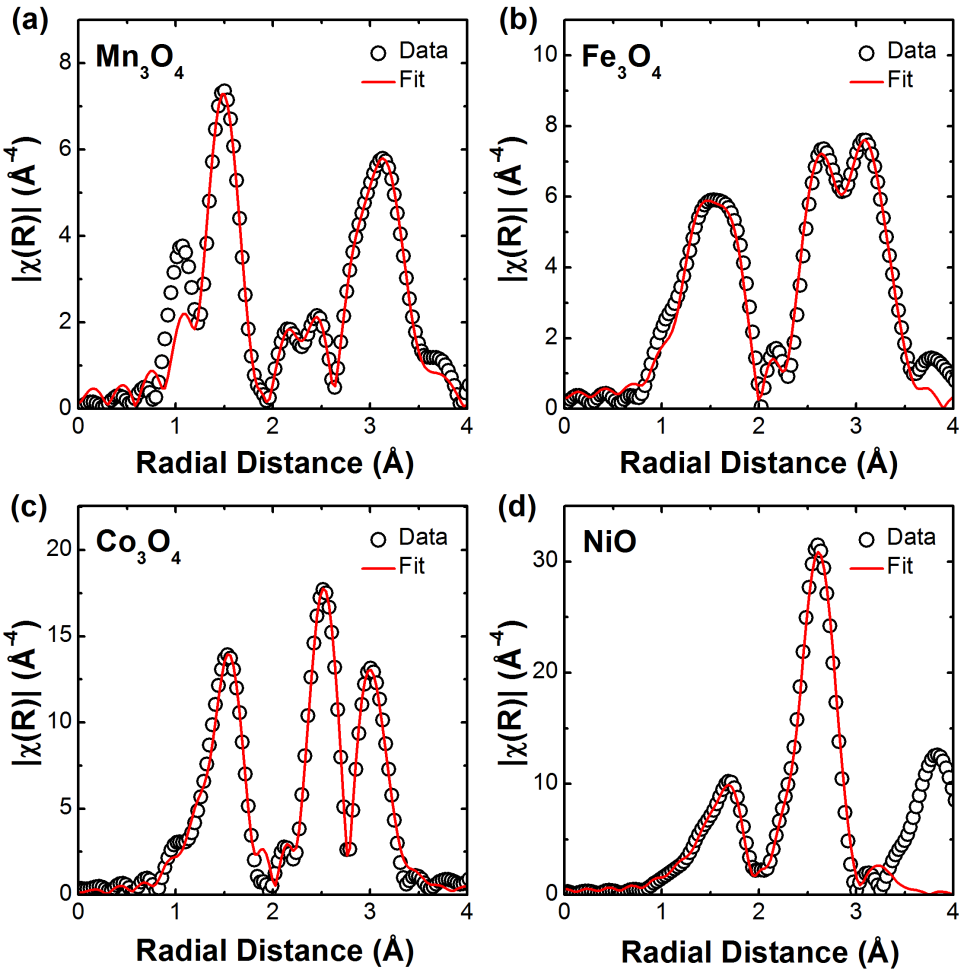


**Figure S16**. EXAFS $k^3\chi(R)$ spectra and fitting results of standard reference samples: (a) $Mn_3O_4$; (b) $Fe_3O_4$; (c) $Co_3O_4$; (d) NiO.

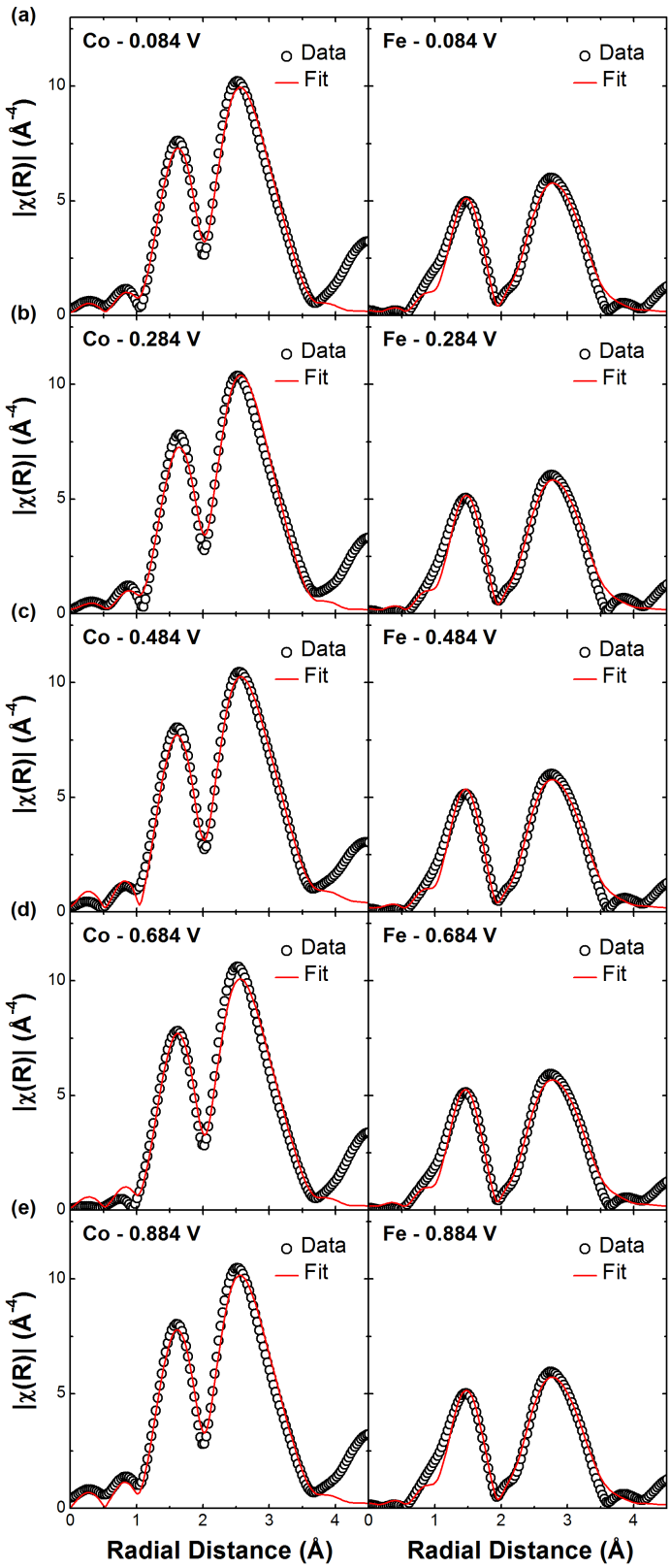


**Figure S17**. In-situ EXAFS $k^3\chi(R)$ spectra and fitting results of $CoFe_2O_4$ at Co and Fe K edge. (a) 0.084 V; (b) 0.284 V; (c) 0.484 V; (d)0.684 V; (d) 0.884 V.

**Table S1. Summary of *in situ* EXAFS fitting results for $MnFe_2O_4$ under different applied potentials.**

| $E_{applied}$ (V) | | 0.084 | 0.284 | 0.484 | 0.684 | 0.884 |
|---|---|---|---|---|---|---|
| Tetrahedral site | $x_{Mn}$ | 0.513 | 0.513 | 0.513 | 0.513 | 0.513 |
| | Mn-O (Å) | 1.88 | 1.88 | 1.89 | 1.88 | 1.90 |
| | Mn-O coordination No. | 3.0 | 3.0 | 3.2 | 3.5 | 4.7 |
| | $x_{Fe}$ | 0.487 | 0.487 | 0.487 | 0.487 | 0.487 |
| | Fe-O (Å) | 1.92 | 1.92 | 1.92 | 1.92 | 1.92 |
| | Fe-O coordination No. | 3.0 | 3.0 | 3.0 | 3.0 | 2.9 |
| Octahedral site | $y_{Mn}$ | 0.487 | 0.487 | 0.487 | 0.487 | 0.487 |
| | Mn-O (Å) | 2.01 | 2.01 | 2.01 | 2.01 | 2.03 |
| | Mn-O coordination No. | 4.4 | 4.5 | 4.6 | 5.06 | 6.6 |
| | $y_{Fe}$ | 1.513 | 1.513 | 1.513 | 1.513 | 1.513 |
| | Fe-O (Å) | 1.99 | 1.99 | 1.99 | 1.99 | 1.99 |
| | Fe-O coordination No. | 4.5 | 4.5 | 4.4 | 4.5 | 4.4 |

**Table S2. Summary of EXAFS fitting: statistical data for $XFe_2O_4$ (X = Mn, Fe, Co, Ni) and reference samples.**

| S/N | Sampe | $\chi^2_\upsilon$ | *R* factor |
|---|---|---|---|
| 1 | $Fe_3O_4$ | 103.7 | 0.0076 |
| 2 | $Co_1Fe_2O_4$ | 376.9 | 0.0188 |
| 3 | $Ni_1Fe_2O_4$ | 674.1 | 0.0548 |
| 4 | $Mn_1Fe_2O_4$ - 200 $^oC$ | 413.8 | 0.0054 |
| 6 | $Mn_1Fe_2O_4$ - 300 $^oC$ | 382.3 | 0.0171 |
| 5 | $Mn_1Fe_2O_4$ - 400 $^oC$ | 263.3 | 0.0211 |
| 7 | $Mn_1Fe_2O_4$ – 0.084 V | 204.9 | 0.0065 |
| 8 | $Mn_1Fe_2O_4$ – 0.284 V | 246.1 | 0.0063 |
| 9 | $Mn_1Fe_2O_4$ – 0.484 V | 193.5 | 0.0069 |
| 10 | $Mn_1Fe_2O_4$ – 0.684 V | 237.1 | 0.0069 |
| 11 | $Mn_1Fe_2O_4$ – 0.884 V | 258.5 | 0.0084 |
| 12 | $Co_1Fe_2O_4$ – 0.084 V | 575.5 | 0.0163 |
| 13 | $Co_1Fe_2O_4$ – 0.284 V | 596.2 | 0.0207 |
| 14 | $Co_1Fe_2O_4$ – 0.484 V | 559.1 | 0.0112 |
| 15 | $Co_1Fe_2O_4$ – 0.684 V | 393.6 | 0.0162 |
| 16 | $Co_1Fe_2O_4$ – 0.884 V | 391.5 | 0.0167 |
| 17 | $Mn_3O_4$ (reference sample) | 282.0 | 0.0027 |
| 18 | $Fe_3O_4$ (reference sample) | 243.3 | 0.0064 |
| 19 | $Co_3O_4$ (reference sample) | 380.8 | 0.0070 |
| 20 | NiO (reference sample) | 525.8 | 0.0055 |

**Table S3. Summary of specific surface area for $XFe_2O_4$ (X = Mn, Fe, Co, Ni).**

| S/N | Sampe | Surface area ($m^2/g$) |
|---|---|---|
| 1 | $Fe_3O_4$ | 166.2 |
| 2 | $Co_1Fe_2O_4$ | 130.3 |
| 3 | $Ni_1Fe_2O_4$ | 113.5 |
| 4 | $Mn_1Fe_2O_4$ - 200 $^oC$ | 150.6 |
| 6 | $Mn_1Fe_2O_4$ - 300 $^oC$ | 133.8 |
| 5 | $Mn_1Fe_2O_4$ - 400 $^oC$ | 114.9 |

**Table S4. Summary of EXAFS fitting results for $XFe_2O_4$ (X = Fe, Co, Ni).**

| sample | | $Fe_3O_4$ | $CoFe_2O_4$ | $NiFe_2O_4$ |
|---|---|---|---|---|
| Tetrahedral site | $x_x$ | n.a. | 0.109 | 0.120 |
| | X-O (Å) | n.a. | 1.81 | 1.93 |
| | X-O coordination No. | n.a. | 3.3 | 3.2 |
| | $x_{Fe}$ | 1 | 0.891 | 0.880 |
| | Fe-O (Å) | 1.87 | 1.93 | 1.93 |
| | Fe-O coordination No. | 3.3 | 3.0 | 2.9 |
| Octahedral site | $y_x$ | n.a. | 0.891 | 0.880 |
| | X-O (Å) | n.a. | 2.06 | 2.03 |
| | X-O coordination No. | n.a. | 4.9 | 4.7 |
| | $y_{Fe}$ | 2 | 1.109 | 1.120 |
| | Fe-O (Å) | 1.98 | 1.99 | 1.96 |
| | Fe-O coordination No. | 5.0 | 4.5 | 4.4 |

**Table S5. Summary of EXAFS fitting results for $Mn_1Fe_2O_4$ synthesized under different temperautre.**

| $Mn_1Fe_2O_4$ sample | | 200 °C | 300 °C | 400 °C |
|---|---|---|---|---|
| Tetrahedral site | $x_{Mn}$ | 0.513 | 0.304 | 0.091 |
| | Mn-O (Å) | 1.88 | 1.84 | 1.73 |
| | Mn-O coordination No. | 2.9 | 3.3 | 3.2 |
| | $x_{Fe}$ | 0.487 | 0.696 | 0.909 |
| | Fe-O (Å) | 1.82 | 1.82 | 1.84 |
| | Fe-O coordination No. | 3.4 | 3.2 | 3.3 |
| Octahedral site | $y_{Mn}$ | 0.487 | 0.696 | 0.909 |
| | Mn-O (Å) | 2.02 | 1.94 | 1.94 |
| | Mn-O coordination No. | 4.3 | 4.9 | 4.8 |
| | $y_{Fe}$ | 1.513 | 1.304 | 1.091 |
| | Fe-O (Å) | 1.99 | 1.99 | 2.00 |
| | Fe-O coordination No. | 5.0 | 4.8 | 4.9 |

**Table S6. Summary of *in situ* EXAFS fitting results for $CoFe_2O_4$ under different applied potentials.**

| $E_{applied}$ (V) | | 0.084 | 0.284 | 0.484 | 0.684 | 0.884 |
|---|---|---|---|---|---|---|
| Tetrahedral site | $x_{Co}$ | 0.109 | 0.109 | 0.109 | 0.109 | 0.109 |
| | Co-O (Å) | 1.81 | 1.80 | 1.80 | 1.81 | 1.81 |
| | Co-O coordination No. | 3.4 | 3.4 | 3.5 | 3.5 | 3.6 |
| | $x_{Fe}$ | 0.891 | 0.891 | 0.891 | 0.891 | 0.891 |
| | Fe-O (Å) | 1.93 | 1.93 | 1.92 | 1.92 | 1.93 |
| | Fe-O coordination No. | 3.0 | 3.0 | 3.0 | 3.0 | 3.0 |
| Octahedral site | $y_{Co}$ | 0.891 | 0.891 | 0.891 | 0.891 | 0.891 |
| | Co-O (Å) | 2.06 | 2.06 | 2.07 | 2.06 | 2.06 |
| | Co-O coordination No. | 5.2 | 5.1 | 5.1 | 5.3 | 5.4 |
| | $y_{Fe}$ | 1.109 | 1.109 | 1.109 | 1.109 | 1.109 |
| | Fe-O (Å) | 1.99 | 1.99 | 1.98 | 1.98 | 1.99 |
| | Fe-O coordination No. | 4.5 | 4.5 | 4.5 | 4.5 | 4.5 |

**Table S7. EXAFS fitting results of M – M interaction for $MnFe_2O_4$-200 $^oC$.**

| Mn K-edge | | | Fe K-edge | | |
|---|---|---|---|---|---|
| Path | R (Å) | $\sigma^2$ | Path | R (Å) | $\sigma^2$ |
| Tetrahedral site | | | Tetrahedral site | | |
| $Mn_A - M_B$ | 3.52 | 0.010 | $Fe_A - M_B$ | 3.52 | 0.015 |
| $Mn_A - M_A$ | 3.67 | 0.003 | $Fe_A - M_A$ | 3.67 | 0.009 |
| Octahedral site | | | Octahedral site | | |
| $Mn_B - M_B$ | 3.00 | 0.007 | $Fe_B - M_B$ | 3.00 | 0.009 |
| $Mn_B - M_A$ | 3.52 | 0.010 | $Fe_B - M_A$ | 3.52 | 0.015 |

∗ $M_A$ denotes the metal cations that locate at the tetrahedral sites; $M_B$ denotes the metal cations that locate at the octahedral sites. For example, $Mn_A - M_B$ denotes the path between the tetrahedral-coordinated Mn cations and octahedral-coordinated metal cations; the absorber is the tetrahedral-coordinated Mn cation

**Table S8. EXAFS fitting results of M – M interaction for $MnFe_2O_4$-300 $^oC$.**

| Mn K-edge | | | Fe K-edge | | |
|---|---|---|---|---|---|
| Path | R (Å) | $\sigma^2$ | Path | R (Å) | $\sigma^2$ |
| Tetrahedral site | | | Tetrahedral site | | |
| $Mn_A - M_B$ | 3.48 | 0.011 | $Fe_A - M_B$ | 3.48 | 0.008 |
| $Mn_A - M_A$ | 3.63 | 0.007 | $Fe_A - M_A$ | 3.63 | 0.005 |
| Octahedral site | | | Octahedral site | | |
| $Mn_B - M_B$ | 2.97 | 0.007 | $Fe_B - M_B$ | 2.97 | 0.010 |
| $Mn_B - M_A$ | 3.48 | 0.011 | $Fe_B - M_A$ | 3.48 | 0.008 |

**Table S9. EXAFS fitting results of M – M interaction for $MnFe_2O_4$-400 $^oC$.**

| Mn K-edge | | | Fe K-edge | | |
|---|---|---|---|---|---|
| Path | R (Å) | $\sigma^2$ | Path | R (Å) | $\sigma^2$ |
| Tetrahedral site | | | Tetrahedral site | | |
| $Mn_A - M_B$ | 3.48 | 0.012 | $Fe_A - M_B$ | 3.48 | 0.010 |
| $Mn_A - M_A$ | 3.64 | 0.022 | $Fe_A - M_A$ | 3.64 | 0.023 |
| Octahedral site | | | Octahedral site | | |
| $Mn_B - M_B$ | 2.97 | 0.011 | $Fe_B - M_B$ | 2.97 | 0.009 |
| $Mn_B - M_A$ | 3.48 | 0.012 | $Fe_B - M_A$ | 3.48 | 0.010 |

**Reference**


(1) Xu, Z.; Shen, C.; Hou, Y.; Gao, H.; Sun, S. *Chem. Mater.* **2009**, *21*, 1778.
(2) Yan, J.; Fan, Z.; Wei, T.; Qian, W.; Zhang, M.; Wei, F. *Carbon* **2010**, *48*, 3825.
(3) Wei, C.; Lee, P. S.; Xu, Z. *RSC Adv.* **2014**, *4*, 31416.
(4) Lee, S. W.; Kim, J.; Chen, S.; Hammond, P. T.; Shao-Horn, Y. *ACS Nano* **2010**, *4*, 3889.
(5) Calvin, S.; Carpenter, E. E.; Ravel, B.; Harris, V. G.; Morrison, S. A. *Phys. Rev. B* **2002**, *66*, 224405.
(6) Nilsen, M. H.; Nordhei, C.; Ramstad, A. L.; Nicholson, D. G.; Poliakoff, M.; Cabañas, A. *J. Phys. Chem. C* **2007**, *111*, 6252.
(7) Carta, D.; Casula, M. F.; Falqui, A.; Loche, D.; Mountjoy, G.; Sangregorio, C.; Corrias, A. *J. Phys. Chem. C* **2009**, *113*, 8606.
(8) Vamvakidis, K.; Katsikini, M.; Sakellari, D.; Paloura, E. C.; Kalogirou, O.; Dendrinou-Samara, C. *Dalton Trans.* **2014**, *43*, 12754.
(9) Wu, G.; Wang, J.; Ding, W.; Nie, Y.; Li, L.; Qi, X.; Chen, S.; Wei, Z. *Angew. Chem. Int. Ed.* **2016**, *55*, 1340.